

XMM-Newton

Status of the RGS Calibration

XMM-SOC-CAL-TN-0030 Issue 6.0
A.M.T. Pollock on behalf of the RGS consortium

2011 February 18

Contents

1	Introduction	3
2	The RGS Calibration	5
2.1	Effective area	7
2.1.1	Empirical effective-area corrections	8
2.1.2	Contamination correction	8
2.1.3	RGS1 dispersion-dependent correction	9
2.1.4	Sensitivity of RGS2 CCD2	9
2.1.5	Instrumental Oxygen absorption	10
2.1.6	Higher-order corrections	11
2.1.7	The final CCF model of the RGS effective area	12
2.1.8	RGS-pn rectification	12
2.2	RGS2 single-node readout	14
2.3	Line spread function	14
2.4	Wavelength scale	17
2.5	Cross-dispersion distribution	17
3	Calibration-related aspects of RGS data analysis	18
3.1	The RGS Background	18
3.2	Pile-up	20
3.3	CCD detector defects	20
3.4	Pixel offset values	20
3.5	Fixed-pattern noise	20

3.6 RGS temporal resolution 21

1 Introduction

The two high-resolution RGS instruments aboard the XMM-Newton Observatory have been operating for eleven years since first light a few weeks after launch in 1999. The set of CCF calibration files that describes the instruments has undergone significant development since then to include in particular time-variable empirical effective area corrections for RGS1 and RGS2 over the 6-38 Å bandwidth. As described in more detail below, these corrections were derived independently for the RGS based on reasonable assumptions concerning the spectral form of a few well-known X-ray sources, and have had the effect of greatly improving the agreement between RGS and the EPIC instruments, the differences between which now conservatively stand at a few percent. An extensive comparison of RGS and EPIC-pn was made in 2010 in an exercise known as RGS-pn rectification.

In addition to the slowly-changing, wavelength-dependent changes in the sensitivity of the RGS, one CCD assembly of the nine in each RGS failed early in the mission because of electronics problems. These were RGS1 CCD7 and RGS2 CCD4, roughly covering the wavelength ranges 11-14Å and 20-24Å, respectively, in first order. Coverage of the wavelengths affected has been maintained by the built-in redundancy between RGS1 and RGS2 or between 1st and 2nd order or both.

Concerning its high-resolution capabilities, measurements of wavelengths are accurate to better than about 7 mÅ. The dramatic reduction of the effects of radiation damage after the operating temperatures of RGS1 and RGS2 were lowered from -80°C to -110°C in November 2002 has been maintained. Otherwise the instruments continue to operate as well as before.

These conclusions are based on SAS analysis of the RGS event files generated from the set of raw data files to be found in the ODFs that are the means by which data are delivered to observers. Raw data ODFs of all calibration observations are available through XSA, the XMM-Newton Science Archive, along with observations whose proprietary data rights have expired. Observers also receive, and others may download from the XSA, high-level scientific RGS products produced by the PPS, an automatic version of the SAS run at the XMM-Newton Science Survey Centre at Leicester University. The purpose of this document is to alert users to the quality of the instrumental calibrations developed so far in order to provide a proper context for the scientific interpretation of RGS data. Documents of varying levels of complexity are available to people interested in the details of the instrument's construction and behaviour: a summary of important instrumental parameters is shown below; a more thorough description of the instrument and the flight performance is given in [1]; and detailed individual calibration documents, written mainly by instrument experts at SRON Utrecht, Columbia University and the XMM-Newton SOC, are available on-line [2, 3] as shown by the list of references at the end of this document.

The RGS delivers high spectral resolution at a sensitivity similar to many low-spectral-resolution X-ray instruments of recent years. The instrumental line width is weakly wavelength dependent with mean FWHM of about 70mÅ and 50mÅ in first and second order, respectively. Pending more detailed discussion below, the overall performance may be summarised thus :

RGS calibrated bandwidth	
	$6 \leq \lambda(\text{\AA}) \leq 38$
	$0.33 \leq E(\text{keV}) \leq 2.07$
Maximum effective area combining RGS1 and RGS2	
1st order	$A \sim 125 \text{ cm}^2$ at 15Å
2nd order	$A \sim 57 \text{ cm}^2$ at 10Å
Wavelength resolution $\lambda/\Delta\lambda$	
1st order	$R \sim 250$ at 15Å
2nd order	$R \sim 300$ at 10Å
Wavelength accuracy	
RGS1	7mÅ
RGS2	7mÅ
Typical full-detector background rates	
6-8Å	$5 \text{ cts ks}^{-1} \text{ \AA}^{-1}$
8-27Å	$2 \text{ cts ks}^{-1} \text{ \AA}^{-1}$
27-34Å	$7 \text{ cts ks}^{-1} \text{ \AA}^{-1}$
34-38Å	$2 \text{ cts ks}^{-1} \text{ \AA}^{-1}$
Time resolution given by CCD integration time	
RGS1	0.6s
RGS2	1.2s

Table 1: Summary of the main characteristics of the XMM-Newton Reflection Grating Spectrometers in standard spectroscopy mode.

2 The RGS Calibration

The instrument calibration is based on a physical model of the various instrument components including

- the mirror response (not part of this document)
- the grating response
 - reflectivity
 - figure errors
 - scattering
 - alignment
 - vignetting
- the CCD detector response
 - quantum efficiency, QE
 - monochromatic pulse-height redistribution function
 - transmission of the optical blocking filter
 - charge transfer inefficiency (CTI)
 - gain

During ground calibrations, these various components were calibrated and a physical model for each constructed and later verified in flight. Subsequent adjustments in the form of time-dependent and wavelength-dependent empirical corrections have been based on in-flight observations of specific sources.

- empirical effective-area corrections
 - assumed power-law blazar spectra
 - detector contamination

The resulting knowledge of the instrument is encapsulated in the set of 14 RGS CCF files shown in Table 2 with some important relevant general-purpose components. There are two CCF files that contain only nominal values that are not used in any analysis. An extensive description of the instrument model is given in [33] and details may also be found in the XMM-Newton User Handbook [31].

During routine operations, many instrumental parameters are monitored, such as detector contamination; detector gain; and CTI evolution due to radiation damage; and this leads to periodic modifications of the relevant RGS CCF components. It should be emphasised that new CCF components may be released at any time, not necessarily coordinated with new versions of the SAS or new issues of this document. Users are strongly recommended to take advantage of one of the automatic synchronisation procedures described on the XMM-Newton web pages [4] that are designed to keep a local set of calibration files up-to-date. Each new CCF component made publicly available is accompanied by a release note with a name of the form XMM-CCF-REL-*nnn* available on the web describing its relevance and applicability.

CCF component	RGS1 vvvv	RGS2 vvvv	Release Note	date
CCD event selection criteria RGS%_ADUCONV_vvvv.CCF	0021	0024	XMM-CCF-REL-214 XMM-CCF-REL-237	2007-12-17 2007-12-17
CCD bad pixels RGS%_BADPIX_vvvv.CCF	0023	0020	XMM-CCF-REL-239 XMM-CCF-REL-226	2007-09-04 2007-03-22
CCD readout parameters RGS%_CLOCKPATTERNS_vvvv.CCF	0001	0001	XMM-CCF-REL-15	2000-09-08
Cross-dispersion PSF parameters RGS%_CROSSPSF_vvvv.CCF	0004	0004	XMM-CCF-REL-142	2002-12-19
CCD CTI correction parameters RGS%_CTI_vvvv.CCF	0009	0010	XMM-CCF-REL-213 XMM-CCF-REL-237	2006-06-29 2007-08-17
CCD dark response RGS%_DARKFRAME_vvvv.CCF	0005	0006	XMM-CCF-REL-173	2004-07-19
CCD effective area correction factors RGS%_EFFAREACORR_vvvv.CCF	0008	0008	XMM-CCF-REL-262	2010-12-17
CCD quantum efficiency correction factors RGS%_EXAFS_vvvv.CCF	0005	0005	XMM-CCF-REL-212	2006-06-27
HK parameter selection criteria RGS%_HKPARMINT_vvvv.CCF	0013	0012	XMM-CCF-REL-134	2002-12-05
RGS system geometry RGS%_LINCOORD_vvvv.CCF	0008	0008	XMM-CCF-REL-81	2001-06-19
Dispersion PSF model component parameters RGS%_LINESPREADFUNC_vvvv.CCF	0004	0004	XMM-CCF-REL-88	2001-09-05
CCD readout parameters RGS%_MODEPARAM_vvvv.CCF	0005	0005	XMM-CCF-REL-15	2000-09-08
CCD quantum efficiency physical model RGS%_QUANTUMEF_vvvv.CCF	0015	0016	XMM-CCF-REL-215	2006-06-29
CCD energy response parameters RGS%_REDIST_vvvv.CCF	0004	0004	XMM-CCF-REL-67	2001-03-30
Observed RGS background templates RGS%_TEMPLATEBCKGND_vvvv.CCF	0006	0008	XMM-CCF-REL-261	2010-04-16
Henke X-ray absorption coefficient tables XMM_ABSCOEFS_0004.CCF			XMM-CCF-REL-77	2001-05-14
Includes RGS Euler angles XMM_BORESIGHT_0013.CCF			XXM-CCF-REL-17	2000-10-04
Includes assorted RGS data XMM_MISCDATA_0019.CCF			XMM-CCF-REL-134	2002-12-05
nominal data only RGS%_BACKGROUND_vvvv.CCF	0001	0001	XMM-CCF-REL-10	2000-09-08
RGS%_CALSOURCEDATA_vvvv.CCF	0001	0001	XMM-CCF-REL-10	2000-09-08

Table 2: RGS components of the XMM-Newton CCF in 2010 December. RGS% shows that there are separate files for RGS1 and RGS2. The RGS cooling in November 2002 required several new calibration files, described as usual in the release notes. RGS-specific version numbers and release notes refer to the latest release while the general-purpose files refer to the latest versions relevant to the RGS. Observers should nevertheless make sure that they have the latest versions for the benefit of all instruments. Please be aware that CCF releases generally occur more often than new editions of this document, for example.

2.1 Effective area

Knowledge of the effective area of the two RGS instruments comes from a combination of ground measurements [39] and observations in flight. It has developed significantly since launch with the introduction of two particularly important additions to the calibration that was originally based on an end-to-end physical model of the whole system. Empirical corrections were first introduced in 2006, based on the assumed power-law form of blazar spectra [25], followed a year later by the recognition of wavelength-dependent sensitivity changes which are consistent with a build-up of hydrocarbon contamination on the cold CCD detector surfaces.

The overall characteristics of the effective area are illustrated in Fig. 1. Obvious features include the two failing CCD readout chains and the effect of a number of hot columns and pixels shown by narrow drops in the effective area. Instrumental oxygen absorption is clearly visible near 23 \AA . Less obvious instrumental features revealed on closer inspection include a shallow Al edge around 8.3 \AA from the blocking filter on top of the CCDs and of Mg and F edges around 9.5 \AA and 17.9 \AA respectively from the MgF_2 isolation layer between the CCD and the blocking filter.

As a result of measurements in flight, the effective-area model incorporates these and a number of other corrections which apply to both RGS1 and RGS2 unless stated otherwise:

- empirical corrections based on power-law blazar spectra;
- absorption in a contamination layer;
- dispersion-dependent corrections in RGS1 only;
- sensitivity adjustment of RGS2 CCD2;
- instrumental Oxygen feature near 23 \AA ;
- instrumental MgF_2 feature near 17.9 \AA ;
- empirical higher-order corrections.

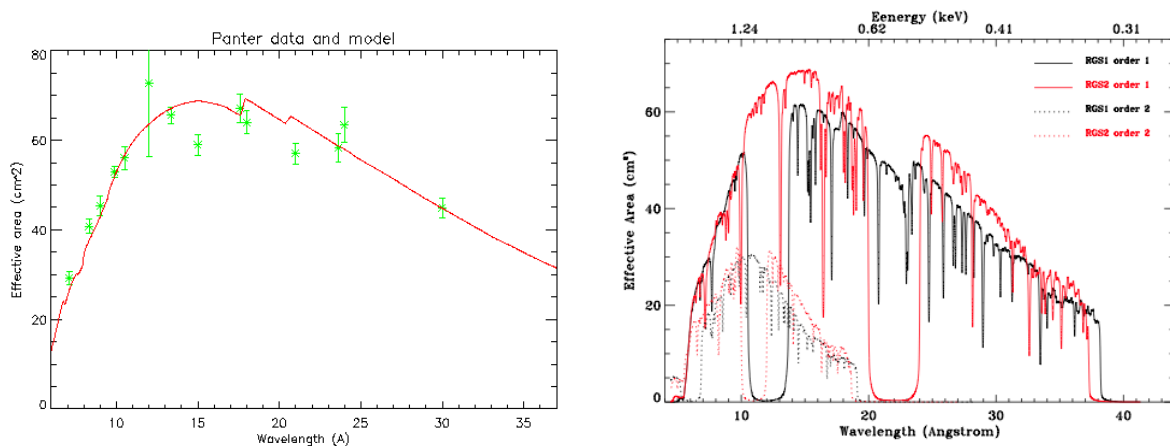


Figure 1: Left: Model of the effective area derived from ground calibrations with a number of measured data points. Right: the CCF in-flight effective area of a typical observation for RGS1 in black and RGS2 in red. Due to scattering the effective area has no sharp features.

2.1.1 Empirical effective-area corrections

The long-wavelength part of the RGS has been difficult to calibrate due to the scarcity of both suitable ground-based facilities and celestial X-ray standards. It has become clear that blazars have smooth spectra well characterised by power-laws subject to interstellar absorption in the RGS waveband. This was empirically supported by the fact that the RGS spectra calculated with earlier versions of the calibration could be corrected for interstellar absorption and power-law slope to reveal a universal form reflecting the shape of the effective area of the RGS instruments. Empirical effective area corrections have been derived using measurements of Mkn421 at different epochs during the mission and fitting a power-law models to the stable, well-calibrated part of the RGS waveband between 10 and 25Å. Using the Crab as a reference for both power-law slope and normalisation, the extrapolation of the resulting models to long and short wavelengths has been used in comparison with the observed spectra to define correction factors. These correction factors are not thought to be time dependent but when combined with the contamination correction discussed immediately below, give rise to the time and wavelength-dependent tabulations in the EFFAREACORR CCFs [18] for the calculation of RGS response matrices. At the shortest wavelengths, the underlying gratings model based on electromagnetic scalar theory breaks down at the small angles involved. This could not be compensated by measurements on the ground and so, at these shortest wavelengths, the empirical correction serves to compensate for the theoretical shortcomings.

2.1.2 Contamination correction

The RGS sensitivity has been decreasing at long wavelengths due almost certainly to the appearance of a layer of contamination on the CCDs. The layer was initially modelled as linearly increasing in thickness [17] but has been increasing more slowly in recent years as shown in Fig. 2 [18]. The exponential law now in place is used to extrapolate into the future and reproduced the observed count rates in the latest calibration observation of RX J1856.6-3754 in late 2010 September to within 3%.

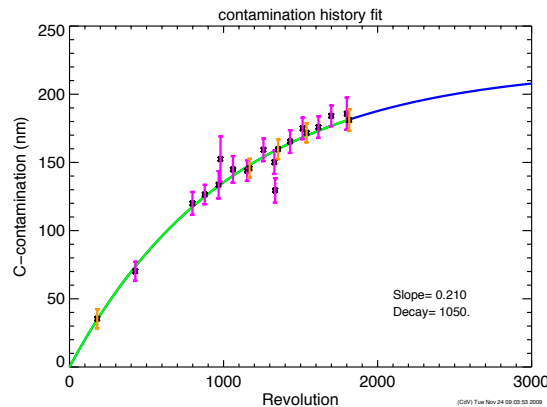


Figure 2: The thickness of the layer of carbon contamination implied by differences in the RGS fluxed spectra of the neutron star RX J1856.6-3754 (pink) and the Vela Pulsar Wind Nebula (orange), both of which are effectively constant. An exponential fit now accounts for the time-variable part of the model of the RGS effective area. Extrapolation into the future is shown by the blue line. The x-axis is time in units of 2-day revolutions or orbits of the XMM-Newton spacecraft around the Earth. XMM-Newton was launched into its 1st revolution on 1999 December 10; revolution 1000 started on 2005 May 25; and revolution 2000 on 2010 November 9.

2.1.3 RGS1 dispersion-dependent correction

Data of calibration sources obtained early in the mission showed unexpected systematic differences between RGS1 and RGS2 with RGS1 20% less efficient at larger dispersion angle, β , than RGS2 as shown in Fig.3. Although not entirely satisfactory in physical terms, this could be explained by additional blocking of the beam halfway between the gratings and the detectors - although the required mismatch of the optical blocking shield by 5cm in one of the two instruments would seem unrealistic. In any case, an empirical β -dependent correction ranging from 1.00 at $\beta = 0.040$ rad (6.5 Å for first order) to 1.25 at $\beta = 0.075$ rad (37.7 Å) has been derived [40] and is applied during SAS data analysis.

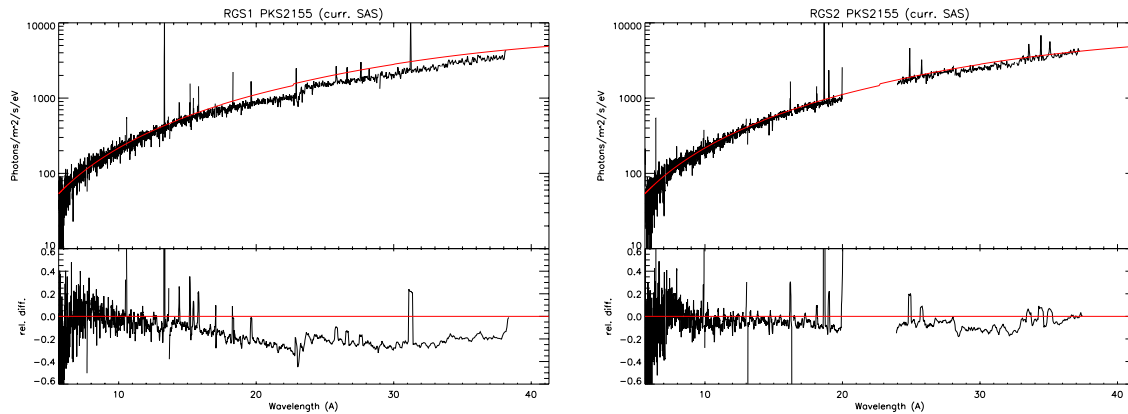


Figure 3: An early fit of PKS2155–304 with the same absorbed power-law spectrum in RGS1 (left) and RGS2 (right). Clearly visible are both the O-edge and the β -dependent RGS1 deficit incorporated into the instrument model.

2.1.4 Sensitivity of RGS2 CCD2

For smooth continuum sources, comparison of the column-dependent count rates of RGS2 CCD2 with its neighbouring CCDs 1 and 3 and with RGS1 CCD2 [40] shows its sensitivity is about 10% lower than expected, likely due to an extra absorbing layer deposited during the manufacturing process. In order to ensure a smooth wavelength-dependent effective area, of various possibilities for an extra passive absorption layer to account for the lower sensitivity of this CCD, a 40nm layer of SiO_2 [7] gives the best description.

2.1.5 Instrumental Oxygen absorption

Around the O-edge there is a significant reduction of about 25 % in the effective area, roughly equivalent to a 30nm layer of Al_2O_3 . Details of this edge, including its fine structure, have been calibrated in flight [41] using a number of sources with low and high column density to separate the detector response from interstellar absorption. Fig. 4 gives both the global structure, that follows the Henke absorption coefficients, and the fine structure. The magnitude of the Oxygen layer on the detector has been confirmed by ground measurements on a flight-spare CCD. Nevertheless, the value of the oxide layer is rather large compared with the two native SiO_2 and Al_2O_3 oxide layers, each of assumed thickness 5nm, so it is plausible that a layer of ice formed on the detector when they were cooled after launch. In addition the 25nm MgF_2 layer is known to be hygroscopic.

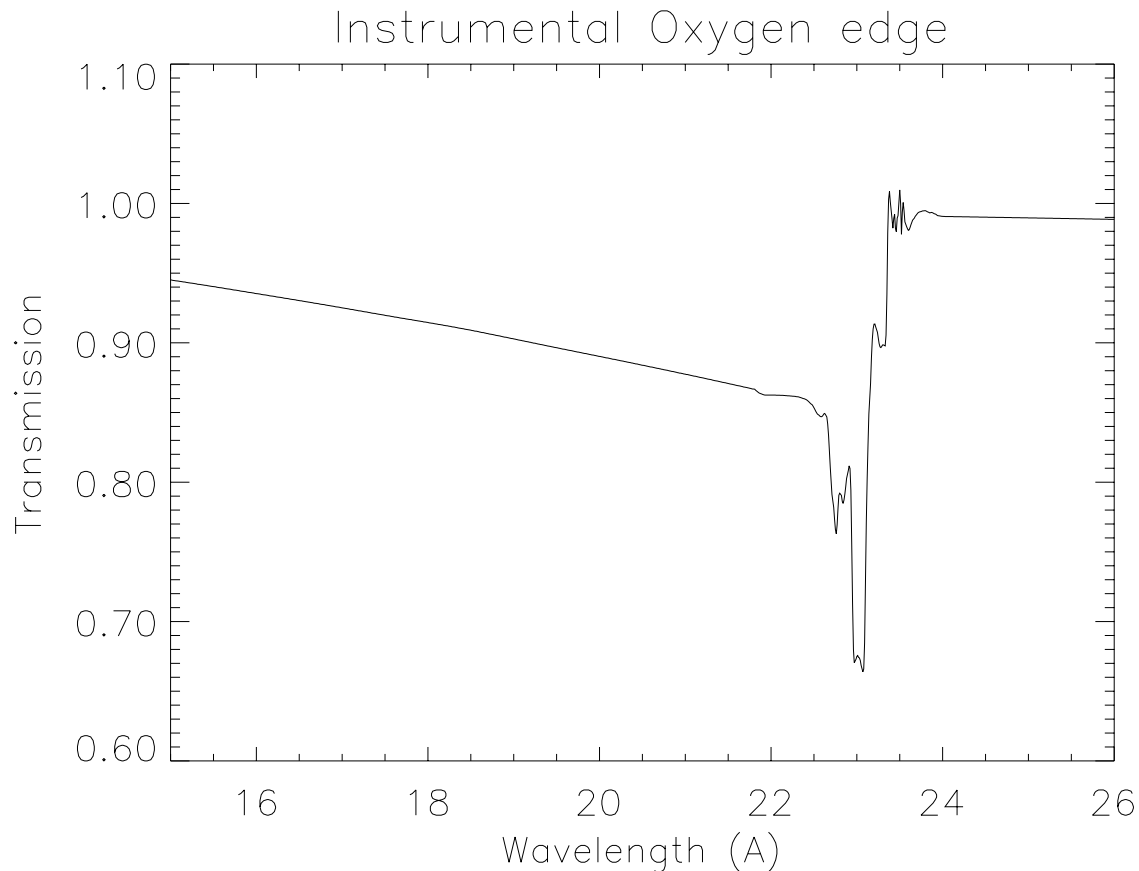


Figure 4: The effect of an additional oxygen layer on the detectors as determined by comparison of sources of varying interstellar column densities.

2.1.6 Higher-order corrections

Between the first and higher spectral orders, wavelength-dependent corrections have been introduced to enforce agreement. Identical correction factors for RGS1 and RGS2 were derived from the relative intensities of Mkn421's first and higher orders as shown in Fig. 5. The largest differences are at low wavelengths where the effective area is small and a steep function of wavelength. It should be emphasised that such efficiency adjustments do not affect the better resolution of the higher orders which can be useful for the identification of lines or the resolution of blends.

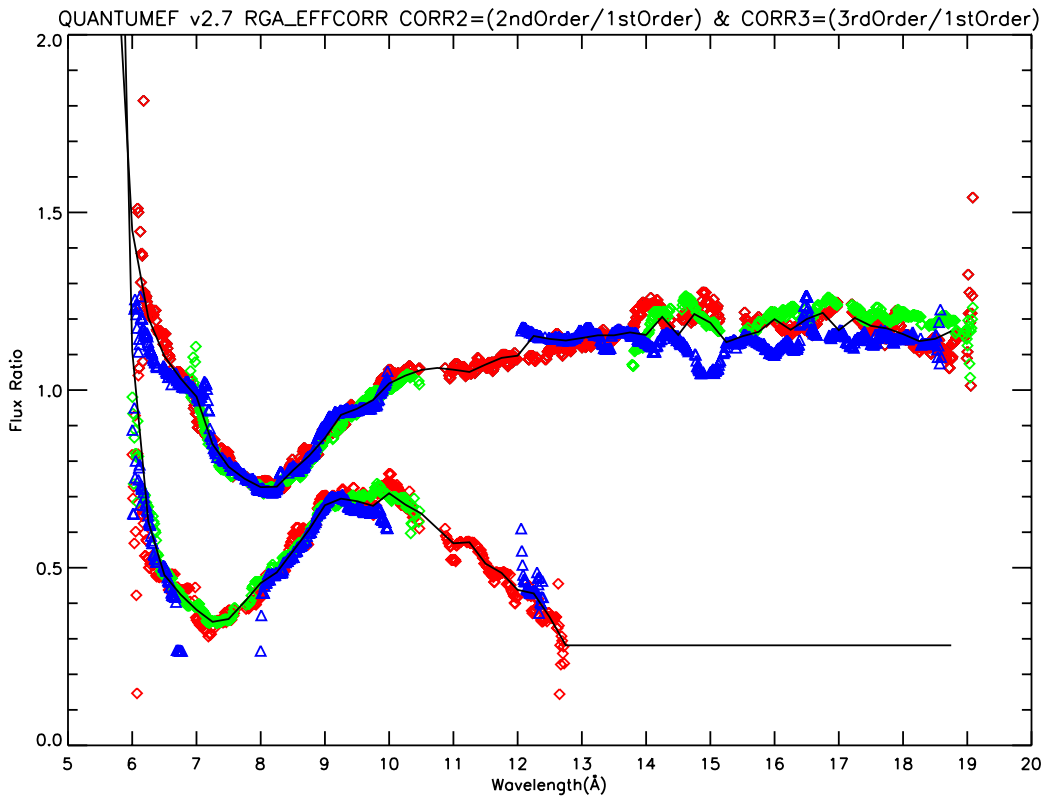


Figure 5: Corrections for 2nd order (above) and 3rd order (below) for the RGS instruments, shown with the solid-line approximations used in the CCF. RGS1 before and after the loss of data from CCD7 is in red and green; RGS2 in blue. See [14] for details.

2.1.1.7 The final CCF model of the RGS effective area

The RGS effective area in an observation is a result of the combination of all the considerations discussed above and thus is a complicated function of time, wavelength and source geometry. Fig. 6 shows how the area at the wavelengths of some prominent ionic emission lines has varied since launch according to the CCF model. The quality of the RGS calibration is best judged by the success of the resulting models in two types of comparison: reproducing the known spectra of calibration standards; and the level of agreement with EPIC on calibration standards and a variety of other objects whose spectra are not known *a priori*. Detailed comparisons of this type using a large sample of observations throughout the mission are described in the XMM-Newton Cross-Calibration Status document [22] and on-line [23].

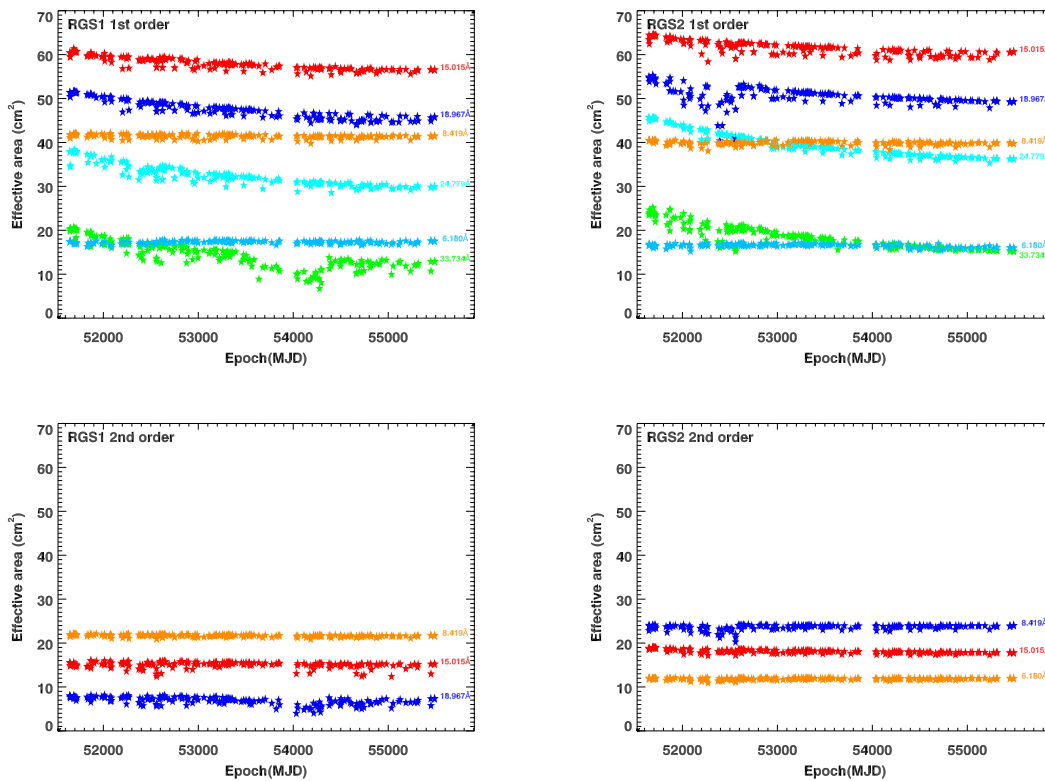


Figure 6: Evolution of the RGS effective area model since launch until 2010-10-11. The points plotted were extracted from the RGS1 and RGS2 1st and 2nd order response matrices calculated with SAS v10.0 of 157 observations in the cross-calibration archive [22, 23] at the XMM-Newton SOC. The effective area is dependent on a combination of conditions and shows, for example, the build up of contamination particularly at long wavelengths; the reduced sensitivity of off-axis measurements; and the significantly fewer bad pixels after cooling the CCDs in 2002 November near MJD52600.

2.1.8 RGS-pn rectification

In 2010, a systematic comparison was made between RGS and EPIC-pn models in an exercise known as RGS-pn rectification [30]. Wavelength-dependent correction factors were applied to RGS models only in spectral analysis of a sample of sources in order to estimate the level of systematic differences between the two instruments which, in the event, were shown to be a few percent. Although these differences are an accumulation of many possible causes including calibration errors in either of the instruments or inadequacies in data analysis or the physical models adopted, a SAS procedure is available [19] to apply rectification factors to RGS RMFs in addition to the best independently-determined calibration in order to improve the consistency of simultaneous analysis of RGS and EPIC-pn data.

2.2 RGS2 single-node readout

On 2007 August 17, the way in which one of the two RGS spectrometers is operated was changed. For several years, RGS2 had been subject to occasional electronics problems with a current limiter during activation at the beginning of some orbits that caused a delay in switching the instrument to its normal spectroscopy mode. Because of the increasing frequency of this condition the decision was made to change the CCD read-out method in RGS2 only from double-node, in which data from the two halves of the RGS2 chips are retrieved separately, to single-node, in which data from the whole chip are read out in through a single amplifier. The first orbit concerned was revolution 1408, when the necessary software and calibration data were in place. As the single-node readout takes twice as long, RGS2 frame times are correspondingly twice as long as those from RGS1. The consequences for pile-up of bright sources is discussed below in section 3.2.

2.3 Line spread function

The monochromatic response, known as the line spread function, results from successive convolutions of the mirror response projected in the dispersion direction; the grating response; and the detector response. The mirror response is approximated by a Lorentzian profile and was calibrated against the flight data of PKS 0312–770 in orbit 057 [34, 6].

Different components contribute to the grating response

- accuracy of the variable line density;
- figure errors;
- misalignments between individual grating elements;
- X-ray scattering by surface roughness.

Two scattering components have been identified corresponding to different scales of the surface roughness: a small-angle Gaussian component and a large-angle Lorentzian component. This scattering is mainly a function of β , the outgoing angle from the gratings in the dispersion direction, but has also a component in χ , the cross-dispersion angle. For each order, β is related to wavelength through the diffraction equation

$$m\lambda = d(\cos \beta - \cos \alpha)$$

where α is the incident angle on the gratings and d is the line spacing. The LSF components in the dispersion direction are illustrated in Fig. 7 where small-angle scattering causes the additional broadening at a few percent of the peak intensity and large-angle scattering dominates at larger distances from the core. Finally, the wings in the line-spread function were reduced by applying an energy selection in the CCD response. The effect of this selection is asymmetric as can be seen in Fig. 7 where the CCD boundaries are also clearly visible.

The LSF was compared early in the mission [35] with lines observed in a number of stellar coronae with agreement between model and data after modification of the instrument model to include a scaling factor applied to the pre-flight grating misalignment distribution of RGS1. This forms the basis for the RGS response matrices calculated by the SAS and for the comparison of observed and predicted line profiles. Experience has shown that the observed lines profiles are usually well reproduced except for the sharp core in some strong lines. Fig. 8 shows an example fit to a coronal OVIII $\lambda\lambda 18.9671, 18.9726$ line showing errors in the core that can give rise, for example, to a formally unacceptable fit in XSPEC for lines of high enough statistical weight.

Although several components of differing angular scales contribute to the complex shape of the LSF, the FWHM gives a rough measure of the instrument's performance. The empirically-determined width of strong, relatively isolated emission lines observed in coronal spectra is a slowly-varying function of

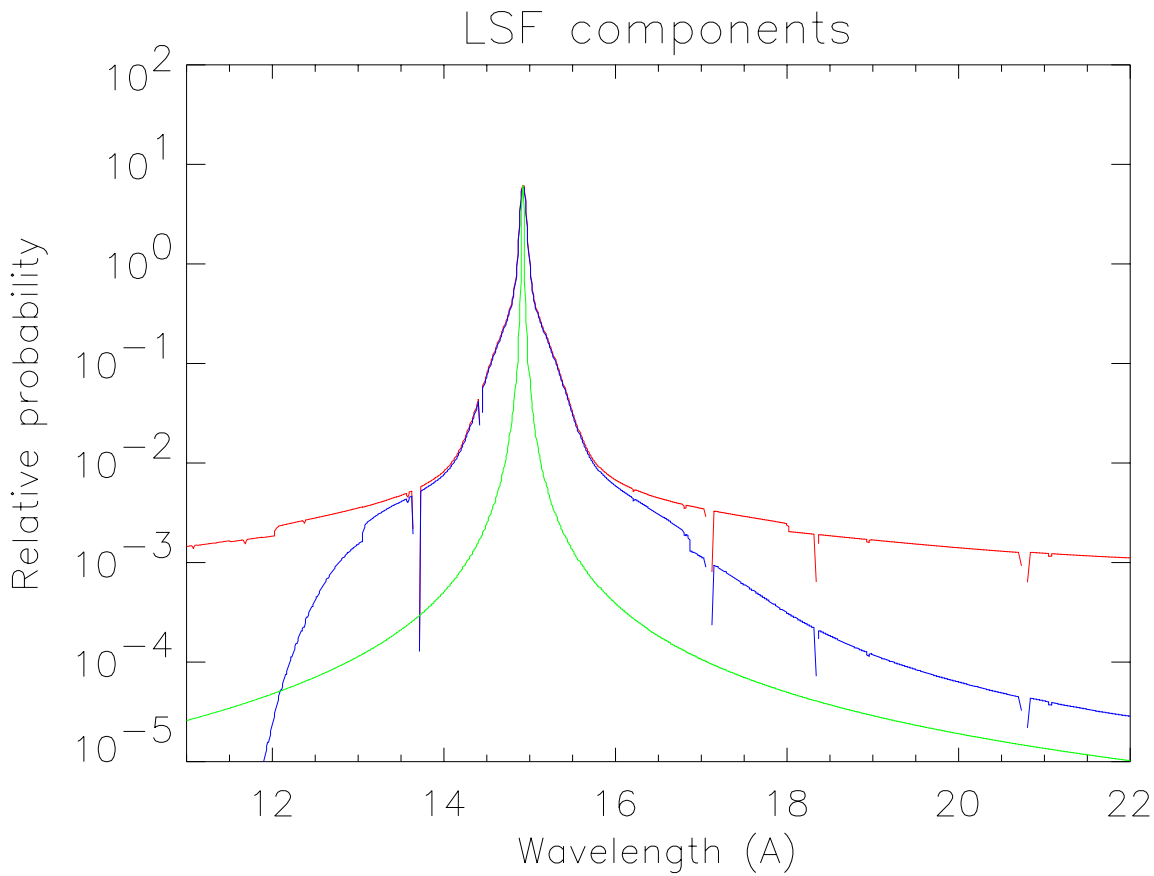


Figure 7: The three main components of the response, known as the LSF, of the RGS to a monochromatic line at 15Å: the projected mirror response is shown in green; after broadening by the grating response in red; and after application of the energy selections to reduce the wings in blue. The small discontinuities near 10^{-3} are due to an approximation used in the numerical treatment of the small-angle scattering.

wavelength in both RGS1 and RGS2 with mean FWHM of about 70mÅ in first order and 50mÅ in second order giving a spectral resolution $\lambda/\Delta\lambda$ that increases with wavelength with typical values of a few hundred. Because of the narrow core mentioned above, observed FWHM are narrower than those of the theoretical CCF LSFs, by median values of 7% and 9% in RGS1 and RGS2, respectively. The release of an improved LSF model is planned in 2011.

To give a more concrete example, Fig. 9 shows data around a coronal NeIX He-like triplet, showing the ability of the RGS to resolve these lines. At longer wavelengths, the He-like triplets of OVII and NVI are comfortably resolved. At shorter wavelengths, MgXI and SiXIII are more difficult to separate.

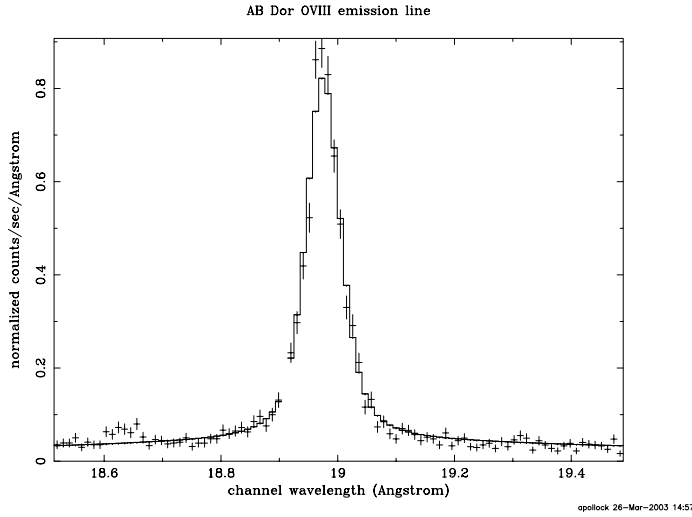


Figure 8: The OVIII Lyman α line in the RGS spectrum of the active star AB Dor, showing data points with error bars and a model fit with a single narrow line. The observed width is of instrumental origin.

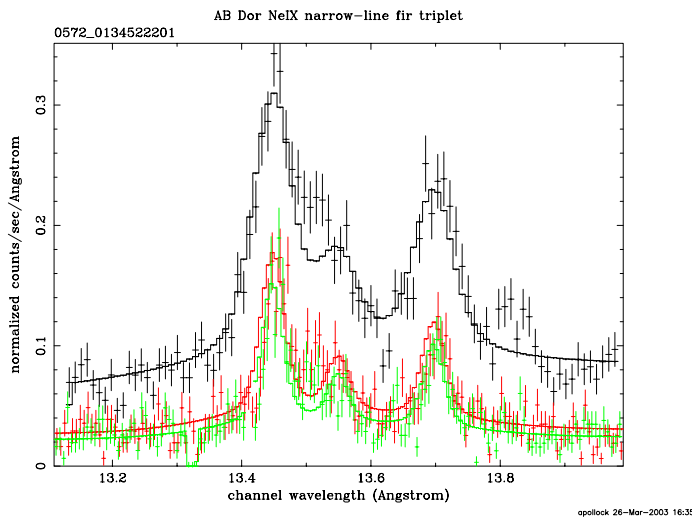


Figure 9: Small parts of the RGS spectra of AB Dor near the NeIX *fir* triplet showing data and errors from RGS2 1st order in black and the higher-resolution 2nd orders of RGS1 and RGS2 in red and green, respectively. The solid lines show a simple model of a narrow-lined triplet and continuum. The excesses near 13.5 Å and 13.8 Å are due to FeXIX, which was not included in the model.

2.4 Wavelength scale

The wavelength scale is determined by the geometry of the various instrument components. While the relative positions of the 9 individual CCDs in each RGS instrument are known to high accuracy from measurements made during instrument integration, the overall instrument orientation and position of the camera reference points were subject to verification in flight using measurements of strong emission lines [20]. After these adjustments, the wavelength scale shows RMS residuals of $\pm 7\text{m}\text{\AA}$ and with the small offsets for RGS1 and RGS2 in first and second order shown in Fig. 10. Subsequent work using many more lines in more observations has confirmed these measurements and allowed an accurate assessment of the misalignment between RGS1 and RGS2 [27, 28]. Alignment of the axes is in work planned for 2011.

As a rule of thumb, every 1 arcsecond error in source coordinates causes a systematic error of $2\text{m}\text{\AA}$ in the wavelength scale, emphasising the importance of using as accurate positions as possible in data analysis. The indications are that the $\pm 7\text{m}\text{\AA}$ residuals quoted above can be improved.

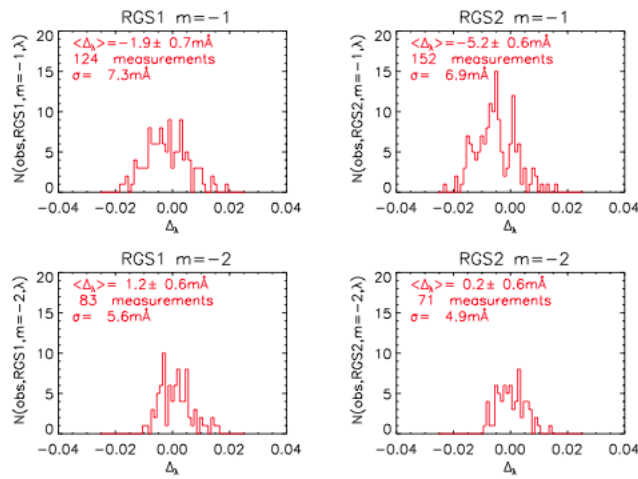


Figure 10: The differences, Δ_λ in \AA , between the observed and laboratory wavelengths of a variety of narrow lines from measurements throughout the mission of 3 stellar coronae in first and second order for RGS1 and RGS2.

2.5 Cross-dispersion distribution

The distribution in the orthogonal cross-dispersion direction is somewhat different from the optimum mirror PSF as the detector follows the Rowland circle in the dispersion direction, which is not ideal for the mirror response, so an empirical determination is made instead. The cross-dispersion distribution of the smooth continuum of the X-ray bright blazar Mkn 421 has been parameterized [9] as a function of the dispersion angle β . This distribution is important as it provides the basis for the SAS to determine selection regions during calculation of point-source spectra.

3 Calibration-related aspects of RGS data analysis

3.1 The RGS Background

In the instrumental background various components have been identified [36, 42] due to

- minimum ionizing particles
- low-energy electrons
- fluorescence lines from the housing
- soft protons entering through the mirrors
- calibration sources
- read-out noise

The net effect of this background can be illustrated using data from the Lockman Hole field which is blank for the RGS. The data shown in Fig. 11 were integrated over the *full* cross-dispersion direction of the detector for periods of a low soft-proton background. In general for point sources, the background can be reliably estimated from parts of the detector in the cross-dispersion direction outside the source-selection region [5], taking care to exclude the on-board calibration sources which illuminate parts of the CCDs. The locations of these calibration sources were chosen to interfere minimally with astronomical data. For extended sources, which can cover an arbitrarily large fraction of the detector's 5 arcmin cross-dispersion width, background region may be selected by inspection or independently by using the RGS background template files [16, 24].

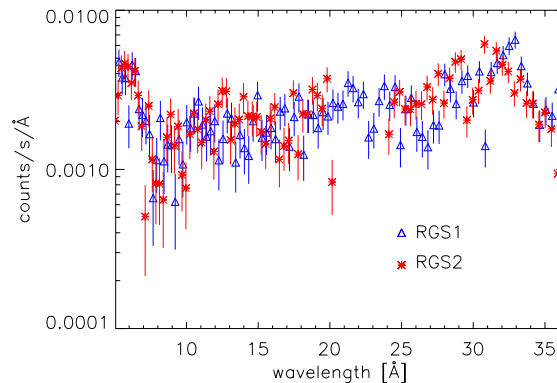


Figure 11: Count rate for the data selections $\{m=-1; 90\%$ in CCD pulse height; all cross-dispersion angles $\}$ for a quiet part of an observation of the Lockman Hole

It is important to point out that the background is sometimes highly variable, as illustrated in Fig. 12. It tends to be strong near the beginning and end of the spacecraft's orbit due to the radiation belts but also to suffer at other times from a highly variable and even overwhelming contribution from soft protons due to solar events which have been known to swamp the astronomical target. It is recommended to use events in CCD9, which is closest to the optical axis, as a monitor to select for processing so-called Good Time Intervals, or GTIs, of low particle background as shown, for example, in section 5.7.2 of the SAS User Guide [32].

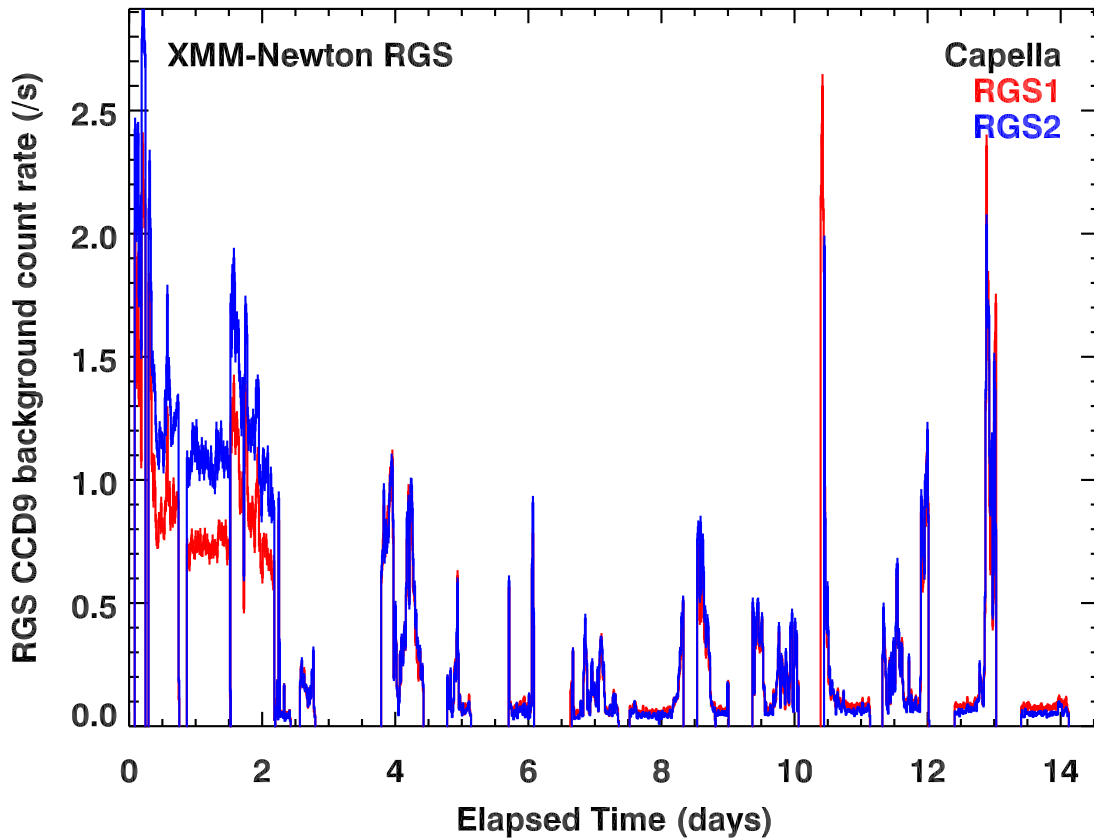


Figure 12: Background count rate from the edges of CCD9 during 18 RGS observations of Capella at different times during the mission. The gaps between individual observations have been logarithmically compressed. Higher background is common at the beginning and end of orbits as the spacecraft enters the outer reaches of the Earth's radiation belts. Otherwise, particle flares may occur at any time. The correlation between RGS1 and RGS2 is usually but not always tight.

3.2 Pile-up

Pile-up is a familiar effect when observing bright X-ray sources with the EPIC instruments, which are non-dispersive and concentrate events from a point source within the small area of the focal plane covered by the PSF. Pile-up occurs when two or more photons are detected in the same pixel during the same integration, in which case they become combined into a single multiple event. This can also happen in the RGS [26] for very bright point sources when, for example, two first-order events arrive in the same pixel close enough in time to be combined into a single apparent second-order photon. The introduction of RGS2 single-node operations discussed above in 2.2 with its longer read-out time has worsened the effect in RGS2. As each RGS pixel suffers a level of pile-up dependent on its individual illumination, it is wise to consider separately line-rich and smooth-continuum sources. Fig. 13 shows the appearance of the strongest lines in the spectrum of Capella in the second order of RGS2 at half their wavelength. Capella is one of the brightest X-ray sources in the sky with a high line-to-continuum ratio so this is more a worst case than a typical example. In the context of the new RGS small-window mode, specifically designed for bright sources, detailed comparison of 1st and 2nd order spectra of Capella [29] showed that pile-up losses amount to a few percent in the brightest lines. For smooth-continuum sources, the pile-up fraction reaches about 2% for CCD count rates of 12 cts/s in RGS1 and 6 cts/s in RGS2. In the rare cases when sources are bright enough for a significant level of pile-up to have occurred, it is not an easy problem to treat, although in the worse cases of which we are aware in the brightest X-ray binaries the pile-up fraction reached no more than 8%. In any case, work is underway on methods that attempt to alleviate the problem in RGS data when it occurs.

3.3 CCD detector defects

Removal of hot pixels and hot columns is a vital part of data analysis, as even a cursory glance at an unfiltered RGS event list will show. While this routine part of the SAS data analysis is usually quite successful, warm or cool - as opposed to hot - pixels that flicker occasionally are sometimes more difficult to detect [37]. Especially for low-intensity sources this may result in distortions of the spectra that, nevertheless, can easily be identified. They are much narrower than the LSF and do not occur in both spectrometers at the same wavelength. In order to enhance the ability to distinguish sometimes subtle absorption or emission spectral features in cosmic sources from detector defects, the RGS offers the Multi-Pointing Mode [31] in which a series of spacecraft repointings are executed automatically in order to move detector blemishes to different parts of the spectrum.

3.4 Pixel offset values

In common with other CCD detectors, offset values are needed to calculate the energy of each detected RGS event. Early in the mission, a single offset value was used for each CCD node. Since SASv6 in 2004, an improved method [21] uses dynamic values calculated for each individual pixel from diagnostic data averaged over three XMM-Newton revolutions. These data are supplied with the ODF and used in RGS data reduction by the SAS with the default switch `withdiagoffset=yes`.

3.5 Fixed-pattern noise

At long wavelengths high-frequency noise can be visible for data with good statistics due to so-called fixed pattern noise in the detector that gives an unmistakable spatial modulation [38]. This can be reduced by either applying somewhat different event reconstruction thresholds or by an improved subtraction of the detector spatial background. Since the introduction of single-node operations, fixed pattern noise in RGS2 has decreased.

3.6 RGS temporal resolution

The instrument's time resolution in spectroscopy mode is determined by the CCD readout procedure. In normal double-node readout for RGS, one CCD is read out every 0.5741s, although this sometimes can reach 0.61s; the full set of 8 CCDs then takes about 4.8s, which is thus the integration time of an individual CCD and the figure that probably best describes the instrument's temporal resolution. For RGS2 single-node operations since 2007 August, the corresponding figures are twice as big, giving a CCD integration time of 9.6s.

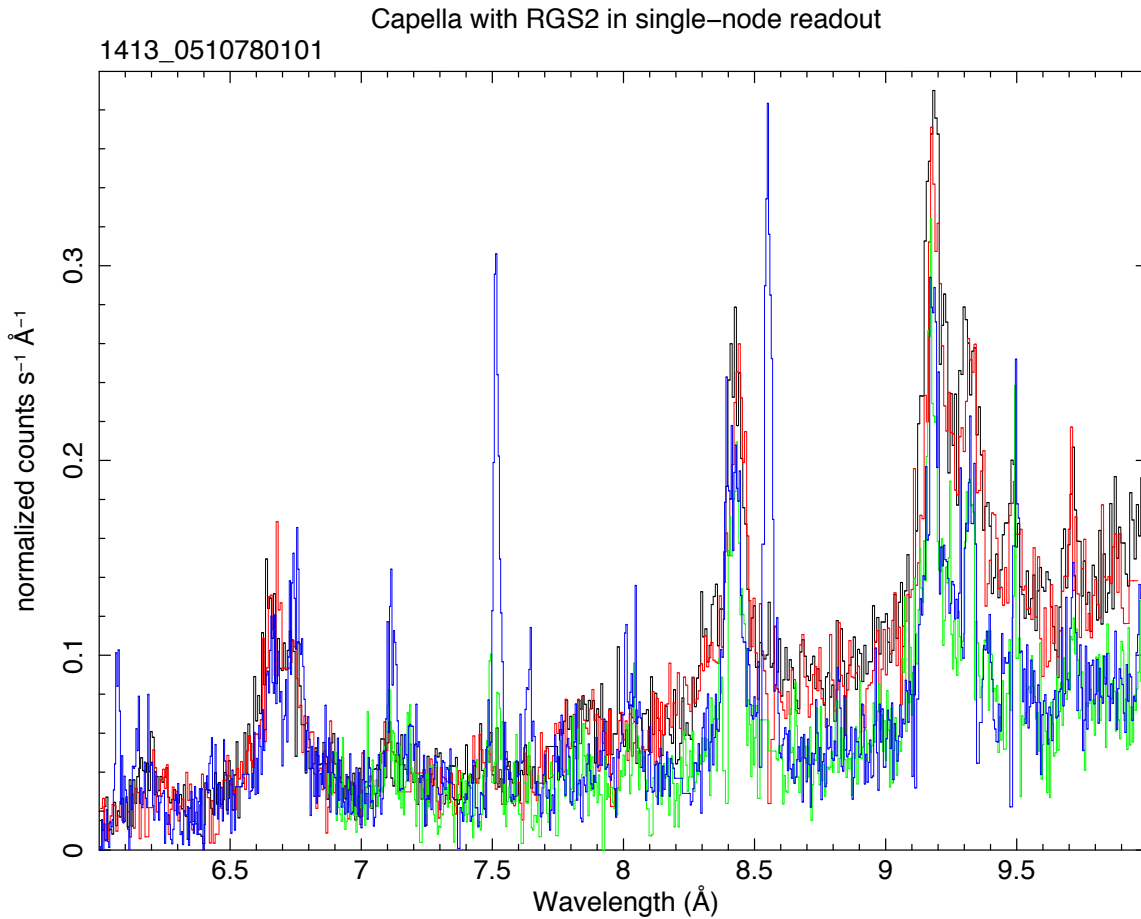


Figure 13: Histograms of the raw data from short-wavelength parts of a Capella spectrum taken since the introduction of RGS2 single-node readout in August 2007. First order spectra of RGS1 and RGS2 are in black and red and the corresponding 2nd orders in green and blue. Errors are not plotted. The 2nd order of RGS2 in blue has clearly been contaminated by pile-up of the strongest lines in the spectrum of FeXVII $\lambda\lambda 15.015, 17.053, 17.096$ and others that show up as spurious features in the 2nd order spectrum at exactly half the wavelength.

- [1] The Reflection Grating Spectrometer on board XMM-Newton, *A&A*, **365**, L7-L17, 2001
- [2] <http://www.sron.nl/divisions/hea/xmm/>
- [3] http://xmm.esac.esa.int/external/xmm_calibration/
- [4] http://xmm2.esac.esa.int/external/xmm_sw_cal/calib/ccf.shtml
- [5] http://xmm.esac.esa.int/external/xmm_user_support/documentation/sas_usg/USG/node99.html
- [6] XRT PSF Parameterization for RGS, XMM-CCF-REL-63
<http://xmm.esac.esa.int/docs/documents/CAL-SRN-0063-1-0.ps.gz>
- [7] RGS2 CCD2 Thickness of SiO₂ Layer, XMM-CCF-REL-71
<http://xmm.esac.esa.int/docs/documents/CAL-SRN-0071-1-0.ps.gz>
- [8] Correcting RGS Quantum Efficiency calibration defects, XMM-CCF-REL-108
<http://xmm.esac.esa.int/docs/documents/CAL-SRN-0108-1-0.ps.gz>
- [9] RGS Cross-Dispersion PSF, XMM-CCF-REL-114
<http://xmm.esac.esa.int/docs/documents/CAL-SRN-0114-1-0.ps.gz>
- [10] RGS QUANTUMEF Shortest-Wavelength Correction Factors, XMM-CCF-REL-176
<http://xmm.esac.esa.int/docs/documents/CAL-SRN-176-1-0.ps.gz>
- [11] Tuning RGS Instrumental MgF₂ Absorption with Mkn421, XMM-CCF-REL-212
<http://xmm.esac.esa.int/docs/documents/CAL-SRN-0212-1-0.ps.gz>
- [12] Evolution of the RGS CTI, XMM-CCF-REL-213
<http://xmm.esac.esa.int/docs/documents/CAL-SRN-0213-1-0.ps.gz>
- [13] Revision of the RGS CCD gains, XMM-CCF-REL-214
<http://xmm.esac.esa.int/docs/documents/CAL-SRN-0214-1-0.ps.gz>
- [14] RGS individual CCD sensitivities and 2nd and 3rd order grating efficiencies, XMM-CCF-REL-215
<http://xmm.esac.esa.int/docs/documents/CAL-SRN-0215-1-0.ps.gz>
- [15] A new model for the RGS effective area, XMM-CCF-REL-216
<http://xmm.esac.esa.int/docs/documents/CAL-SRN-0216-1-0.ps.gz>
- [16] RGS Background Spectra Templates, XMM-CCF-REL-229
<http://xmm.esac.esa.int/docs/documents/CAL-SRN-0229-1-1.ps.gz>
- [17] An improved model the RGS effective area based on the build-up of carbon contamination, XMM-CCF-REL-238
<http://xmm.esac.esa.int/docs/documents/CAL-SRN-0238-1-0.ps.gz>
- [18] The RGS effective area incorporating exponential contamination and a mechanism for rectification, XMM-CCF-REL-262
<http://xmm.esac.esa.int/docs/documents/CAL-SRN-0262-1-0.ps.gz>
- [19] CCF implementation of RGS-pn rectification, XMM-CCF-REL-269
<http://xmm.esac.esa.int/docs/documents/CAL-SRN-0269-2-0.ps.gz>
- [20] The RGS wavelength scale, XMM-SOC-CAL-TN-0041
- [21] System offsets using diagnostic images, XMM-SOC-CAL-TN-0046

- [22] Status of the XMM-Newton Instrument Cross-Calibration, XMM-SOC-CAL-TN-0052
- [23] http://xmm2.esac.esa.int/external/xmm_sw_cal/calib/cross_cal/index.php
- [24] Templates for the RGS Background, XMM-SOC-CAL-TN-0058
- [25] RGS blazar spectra and prospects for an Effective Area correction, XMM-SOC-CAL-TN-0063
- [26] Pileup in RGS spectra, XMM-SOC-CAL-TN-0075
<http://xmm.esac.esa.int/docs/documents/CAL-TN-75-1-0.pdf>
- [27] A Coronal Line Survey for the RGS Wavelength Scale, XMM-SOC-CAL-TN-0079
<http://xmm.esac.esa.int/docs/documents/CAL-TN-79-1-0.pdf>
- [28] Alignment of the RGS1 and RGS2 Wavelength Axes, XMM-SOC-CAL-TN-0080
<http://xmm.esac.esa.int/docs/documents/CAL-TN-80-1-0.pdf>
- [29] RGS small window mode, XMM-SOC-CAL-TN-0086
<http://xmm.esac.esa.int/docs/documents/CAL-TN-86-1-0.pdf>
- [30] An investigation into RGS-pn rectification, XMM-SOC-CAL-TN-0089
<http://xmm.esac.esa.int/docs/documents/CAL-TN-89-1-1.pdf>
- [31] XMM-Newton User's Handbook
http://xmm.esac.esa.int/external/xmm_user_support/documentation/uhb/index.html
- [32] XMM-Newton Science Analysis System User Guide
http://xmm.esac.esa.int/external/xmm_user_support/documentation/sas_usg/USG/SASUSG.html
- [33] Status of the RGS Response, RGS-SRON-CAL-01-005
- [34] The Measured Telescope PSF, RGS-COL-CAL-00003
- [35] Tuning and assessment of the RGS LSF, RGS-COL-CAL-01002
- [36] Model for the RGS background, RGS-COL-CAL-00012
- [37] Hot pixel/column rejection, RGS-COL-CAL-00015
- [38] Fixed pattern noise and flickering pixel rejection, RGS-COL-CAL-01001
- [39] Analysis of RGS FM1 effective area, RGS-SRON-TN-CAL-98-001
- [40] Comparing RGS1 and RGS2, RGS-SRON-CAL-ME-01_cv1
- [41] Instrumental Oxygen edge, RGS-SRON-CAL-ME-01_cv3
- [42] Exposure-to-exposure variation of the RGS background, RGS-SRON-CAL-00-002